International Journal of Solids and Structures 291 (2024) 112717

Contents lists available at ScienceDirect

International Journal of Solids and Structures

journal homepage: www.elsevier.com/locate/ijsolstr

All-atom molecular dynamics simulations of nematic liquid crystal elastomers

Nanang Mahardika [a], Thomas Raistrick [b], L. Angela Mihai [c,*], Haoran Wang [a,*]

[a] Department of Mechanical and Aerospace Engineering, Utah State University, 4130 Old Main Hill, Logan, 84322-4130, UT, United States
[b] School of Physics and Astronomy, University of Leeds, Leeds, LS2 9JT, United Kingdom
[c] School of Mathematics, Cardiff University, Senghennydd Road, Cardiff, CF24 4AG, United Kingdom

ARTICLE INFO

Dataset link: https://doi.org/10.26078/6170-d520

Keywords:
Liquid crystal elastomers
Nematic order parameter
Elastic deformation
Auxeticity
Shape memory
Molecular dynamics

ABSTRACT

Nematic liquid crystal elastomers (LCEs) are advanced materials known for their shape-changing capability in response to external stimuli such as heat, light, solvents and electromagnetic fields. This makes them excellent candidates for applications like soft robotics and energy harvesting. While studies on their physical behavior have shed light on the complex nonlinear mechanics of LCEs, investigations through all-atom molecular dynamics (MD) simulations remain an underutilized avenue compared to experimental and theoretical analyses. This limited use is primarily due to the lack of well-established frameworks for conducting high-fidelity atomistic simulations of LCEs. To bridge this gap, we introduce an all-atom MD simulation framework based on the Polymer Consistent Force-Field (PCFF), which models the polymerization and crosslinking processes for a category of acrylate LCEs and captures their synthesis history- and composition-dependent properties. Our computational framework empowers us to simulate the spontaneous deformations and shape memory behavior upon temperature changes and enables us to observe the auxetic effect under elastic strains by generating models that closely replicate experimental findings. Moreover, this study not only validates the numerical models but opens up new avenues to explore the intricate behaviors of LCEs through their molecular structures and facilitate computational design advancements.

1. Introduction

Liquid crystal elastomers (LCEs) can show significant reversible deformations up to a few hundred percent strains when subjected to external stimuli such as heat, light, solvents or electromagnetic fields (Clarke et al., 2001; Guo et al., 2021; Van Oosten et al., 2007), and are promising materials for applications like robotics and energy harvesting (Rogóż et al., 2016; Stuart et al., 2010; Li et al., 2012). This is due to their advanced structural architecture containing two major building blocks: liquid crystals and polymeric chains. Liquid crystals are typically composed of relatively rigid rod molecules, called mesogens, that are polarized to form long-range orientational order (Warner and Terentjev, 2007). The average direction of all mesogen long axes is termed the director. For example, in thermotropic nematic LCEs, the long-range orientational order can be imprinted into the polymeric network, where liquid crystals are attached, such that a macroscopic shape-memory effect can be achieved upon heating or cooling (Warner and Terentjev, 2007).

The last decade has witnessed a surge in experimental fabrication, characterization, and numerical and theoretical modeling of LCEs (Warner, 2020; Hussain et al., 2021; Mistry, 2021; Soltani et al., 2021; Park et al., 2023). Conventionally, designing and producing LCEs required a background in synthesis chemistry and complicated experimental conditions and was primarily limited to thin films (Ula et al., 2018). The development of versatile 'click' reactions has significantly lowered the technical barriers of LCE synthesis (Saed et al., 2016) and enabled the fabrication of bulk-scale LCEs using 3D printing technology. This further led to promising applications in various disciplines (Ware et al., 2015; de Haan et al., 2014; Kotikian et al., 2019; White and Broer, 2015). At the fundamental level, continuum elasticity theories of LCEs have been developed to capture or predict phenomena such as soft elasticity and shape shifting (Warner and Terentjev, 2007).

In a recent experimental study, Mistry et al. (2018a) reported the observation of an intriguing auxetic response in monodomain acrylate LCEs. When a thin film is stretched perpendicular to the director, its thickness first decreases to a critical tensile strain and then increases while its volume remains unchanged. The critical tensile strain varies from 0.79 to 1.02, depending on the strain rate. Such auxetic behavior has been shown to agree with theoretical model predictions by Mihai

* Corresponding authors.
E-mail addresses: mihaila@cardiff.ac.uk (L.A. Mihai), haoran.wang@usu.edu (H. Wang).

https://doi.org/10.1016/j.ijsolstr.2024.112717
Received 22 November 2023; Received in revised form 6 February 2024; Accepted 9 February 2024
Available online 12 February 2024

et al. (2022, 2023). The emergence of biaxial order is proposed to be the driving force of the auxetic effect (Raistrick et al., 2021; Wang et al., 2022). In a separate study of the same nematic LCE, uniaxial tension tests lead to a three-region stress–strain curve similar to a semi-soft elastic behavior characterized by gradual rotations of the director; however, the 2D optical tracking of the director reveals an apparent sudden rotation of the director, similar to a mechanical-Fréedericksz transition (Mistry et al., 2018b). A later experimental study has revealed that the apparent sudden rotation is because almost all measurement techniques can only resolve a single director, and what likely happens is that minor and major biaxial directors swap at some threshold strain (Wang et al., 2022). These phenomena require more understanding of the LCE behavior at a molecular scale.

Molecular dynamics (MD) simulations are important and promising tools for studying LCEs (Wilson, 2005). A vast majority of existing MD simulations use the Gay-Berne coarse-graining potential (Skačej and Zannoni, 2012; Moon et al., 2019; Whitmer et al., 2013; Brown et al., 2009; Mihai et al., 2021), where mesogens are modeled as ellipsoidal particles with anisotropic interactions. With the coarse-graining potential, the isotropic–nematic phase transition (Ilnytskyi and Neher, 2007; Wilson, 1997) and shape-memory effect of LCEs (Ilnytskyi et al., 2012) are replicated, and their mechanical properties are characterized (Stelzer et al., 1995; Allen et al., 1996; Skacej and Zannoni, 2014). However, these models have been developed for general LCEs to demonstrate certain universal behaviors, and they cannot be relied upon to investigate the composition-dependent behavior of different LCEs. Fewer all-atom MD simulations use force fields such as the general Amber force field (GAFF), Optimized Potentials for Liquid Simulations (OPLS), Dreiding, and Polymer Consistent Force-Field (PCFF) (Boyd and Wilson, 2015; Cheung et al., 2002; Prathumrat et al., 2021). Among them, GAFF, OPLS, and Dreiding force fields tend to overestimate the phase transition or glass transition temperatures; PCFF and its variation predict LCE glass transition temperatures and viscoelastic properties with good accuracy and partially retrieve their spontaneous deformation behavior upon heating. The better performance of PCFF is attributed to its additional cross-coupling terms and the 6–9 LJ potential compared to the 6–12 LJ potential in other force fields (Prathumrat et al., 2021).

Here, we investigate the accuracy of PCFF-based MD simulations with the aim of establishing a high-fidelity computational framework for all-atom MD simulations of LCEs. In the first part, we introduce the MD simulation steps for polymerization and crosslinking to obtain LCEs using PCFF. Our PCFF-based MD simulations demonstrate the shape-memory behavior and auxetic response of acrylate LCEs with great accuracy when validated against experiments. We then analyze the atomistic-level behavior of the MD simulations to understand the underlying physics of the LCE shape-memory and auxetic effects.

This work paves the way for future studies of the process-structure–property correlations and computational design of nematic elastic materials.

2. MD simulations

The LCE computational models in this study are composed of 2-ethylhexyl acrylate (EHA), 6-(4-cyano-biphenyl-4′-yloxy)hexyl acrylate (A6OCB), and 1,4-bis-[4-(6-acryloyloxyhex-yloxy)benzoyloxy]-2-methylbenzene (RM82). The molecular formula of the three monomers and the schematic of their polymerization and crosslinking are shown in Fig. 1(a). Among the three monomers, A6OCB and RM82 are reactive mesogens, which contain rod-shaped rigid parts denoted by the blue and red ellipsoids in Fig. 1(a). The non-mesogenic EHA can increase the flexibility of the polymer backbone. Their molar ratios vary in different models to study the composition-properties relations. In the course of polymerization, the double-bonded carbon atoms located at the terminal reactive sites of monomer molecules establish new bonds with adjacent counterparts in other monomer molecules. This acrylate polymerization process continually progresses, developing an acrylate backbone, as depicted in Fig. 1(a). Notably, RM82 exhibits reactive sites at both ends, enabling it to function as a crosslinker when its two ends are integrated into backbones within different polymer chains.

2.1. Interatomic potential validation

The interatomic potential plays a crucial role in accurately modeling LCEs at the atomistic level. Here, we use the PCFF, which has shown promising results in MD simulations for RM257 and PETMP-based LCEs (Prathumrat et al., 2021). Before delving into simulations of LCE polymerization and crosslinking, we first validate the PCFF by comparing the simulation outcomes of monomers against experimental data. These monomers and their mixtures exhibit consistent properties regardless of their synthesis routes or molecular structures within LCEs. Therefore, they serve as a reliable benchmark to gauge the precision of PCFF-based simulations. We focus on calculating steady-state density ρ and the nematic–isotropic transition temperatures, T_{ni}. Each model comprises 1000 molecules, and we employ an NPT ensemble at 300 K to attain equilibrium under constant pressure of 1 atm for up to 5 nanoseconds (ns). All models reach equilibrium within 2 ns. We obtain ρ from the simulations in the last 1 ns. Table 1 lists densities obtained from MD simulations using PCFF at 300 K for EHA, A6OCB, and RM82. We note that, in general, these simulations using PCFF tend to slightly underestimate monomer densities when compared to experimental values (Lide, 2004).

The T_{ni} is calculated for 5 models with different molar ratios of A6OCB and RM82 monomers. The models are heated to 800 K to remove any orientational order and then quenched to 300 K with an NPT ensemble. During quenching, an electric field is applied to align the mesogens. After 1.5 ns, a stable nematic phase is formed, and the electric field is removed, after which the whole model is equilibrated at 300 K for 5 ns. To quantify the LC order of the models, we use the parameter of S_2, the largest eigenvalue of the molecular ordering tensor below

$$Q_{\alpha\beta}(t) = \frac{1}{N}\sum_{i=1}^{N}[\frac{3}{2}u_{i\alpha}(t)u_{i\beta}(t) - \frac{1}{2}\delta_{\alpha\beta}], \tag{1}$$

where N is the total number of mesogens, $u_{i\alpha}(t)$ and $u_{i\beta}(t)$ are the unit directional vectors of each mesogen's long axis at time t, for $\alpha, \beta = x, y, z$, and the Kronecker delta is $\delta_{\alpha\beta} = 1$ when $\alpha = \beta$, and 0, otherwise. For ideally isotropic liquid crystals, $S_2 = 0$; for ideally nematic liquid crystals, $S_2 = 1$. When applying an electric field of 1 volt/angstrom, S_2 reaches an equilibrium value of 0.8–0.9 within 10 ns, representing a nematic phase. The eventual nematic LC molecules have order ranging from 0.60 to 0.73. Starting from the stable nematic LC monomers at 300 K, we heat the models gradually to observe the evolution of LC order. Fig. 2(a) shows the evolution of LC order with respect to temperatures for A6OCB and RM82 monomer mixtures. Following Maier–Saupe theory (Luckhurst and Zannoni, 1977), we use $S_2 = 0.4$ as the critical LC order for nematic–isotropic phase transition (Boyd and Wilson, 2015), and calculate T_{ni} by linear interpolation. The estimated T_{ni} in Fig. 2(b) are in remarkably good agreement with experimental data obtained from differential scanning calorimetry measurements (Jull et al., 2022). The density and T_{ni} calculations for monomer mixtures exhibit high-fidelity results from PCFF-based MD simulations. Due to the lack of OPLS-based MD simulations of LCEs, we also use OPLS potentials to calculate T_{ni}, which turns out to be 200 K higher than those in experiments. For the monomer mixtures of RM82 and A6OCB, GAFF has been proven robust for predicting their T_{ni} (Jull et al., 2022).

We apply periodic boundary conditions throughout the MD simulations and a cutoff distance of 12 Å for the LJ potential calculations, accounting for both computational accuracy and efficiency. The Coulumbic term is excluded from the interatomic force field for two reasons. First, including the Coulumbic term yields lower phase transition temperatures, which may be caused by inaccurate atomistic

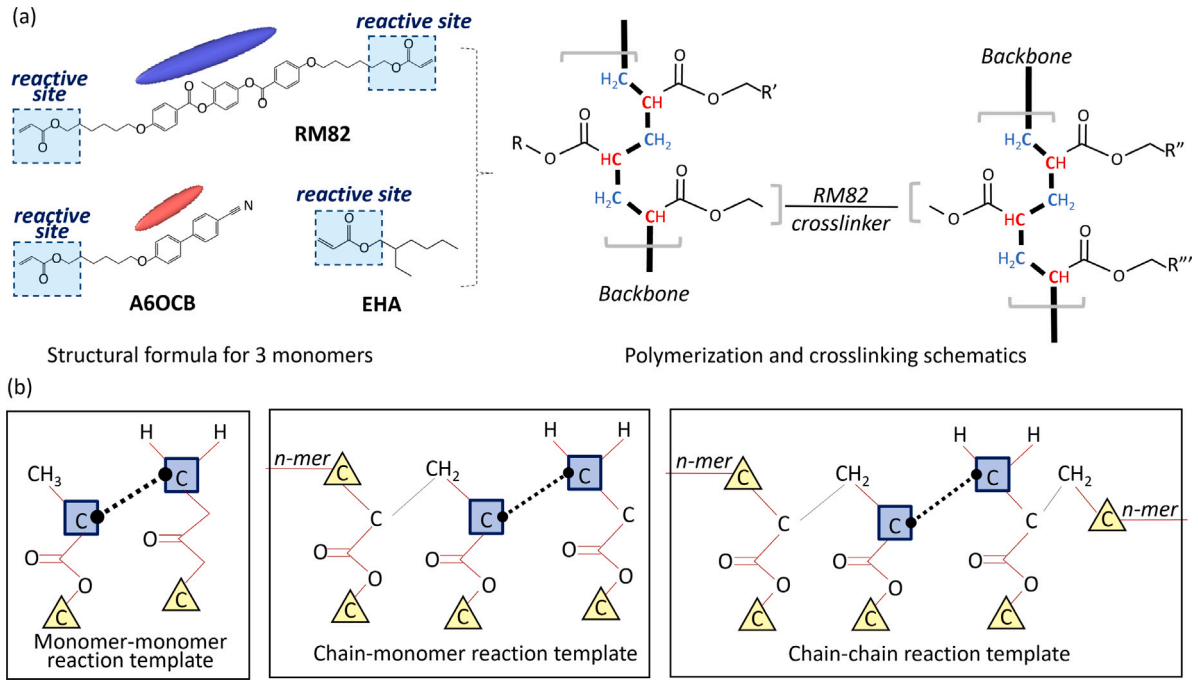

Fig. 1. (a) The chemical structures of RM82, A6OCB, and EHA monomer molecules (left) where the rigid rod-shaped groups in RM82 and A6OCB are represented by blue and red ellipsoids, respectively, and the formation of backbone chains and crosslinking between different chains through the acrylate polymerization between the reactive sites on different monomers (right); (b) the reaction templates for polymerization and crosslinking in MD simulations to generate LCEs, where the C atoms in yellow triangles are the so-called edge atoms connecting with the rest of polymer chains, and the C atoms in blue squares are the so-called initiator atoms between which new bonds form when two initiator atoms are within a critical distance.

Table 1
Steady-state densities of EHA, A6OCB and RM82 monomers (g/cm^3).

Monomers	Experiments (Lide, 2004)	PCFF-based MD simulations	Deviation from experiments
EHA	0.880	0.847	3.70%
A6OCB	1.12 ± 0.1	1.049	Within the range
RM82	1.156	1.120	3.13%

partial charges in our simulations, requiring further investigation. Second, according to Warner and Terentjev (2007), the ordering of liquid crystal molecules is due to the steric effects (shape anisotropy) and thermotropic effects (van der Waals forces), and thus, the Coulombic force is not crucial to the phase transition of LCEs (Warner and Terentjev, 2007).

2.2. Polymerization and crosslinking

The LCE models for MD simulations are created within LAMMPS (Thompson et al., 2022) following the steps below. 1000 molecules of the three monomers are fully mixed in a cube by equilibrating at 800 K with NPT conditions for 0.5 ns. A pressure of 10 MPa is used to prevent void generating in the models. Subsequently, the models are quenched to 500 K, and an electric field is applied to align the mesogens such that a nematic phase of monomers can be established. Then, the polymerization and crosslinking of the monomer molecules are started by using the REACTER module in LAMMPS (Gissinger et al., 2017, 2020). To use this module, we create three reaction templates to model the polymerization and crosslinking at different stages, as shown in Fig. 1(b). The monomer–monomer reaction represents the initiation of the polymerization process. In experiments, the polymerization initiation is activated by photoinitiators. Here, we set a limit of 16 monomer–monomer reactions corresponding to the 1.6 mol% photoinitiators added in experiments (Mistry et al., 2018a). After the monomer–monomer reaction, a short chain is formed. These chains can grow by reacting with monomers, or reacting with other chains, as shown in Fig. 1(b). A cutoff distance of 5 Å is used for polymerization and crosslinking reactions, i.e., when the two initiation atoms in the blue squares in Fig. 1(b) are within 5 Å, the reaction is activated. Using a higher temperature and a relatively larger reaction cutoff distance is necessary to finish the polymerization and crosslinking process in a reasonable time. A smaller timestep of 0.5 femtoseconds (fs) is used to stabilize the polymerization and crosslinking process. For all other MD simulations in this study, we use a time step of 1 fs.

The degree of polymerization, characterized by the number of reacted monomer molecules over all monomer molecules, indicates the progress of polymerization and crosslinking reactions. Fig. 3(a) shows the evolution of the degree of polymerization for models with different compositions. These compositions are chosen because they have experimental results reported by other studies so we can calibrate and validate our simulations. To study the size effect in MD simulations of LCEs, we also include a larger model with 10,000 monomers. When having a lower percentage of RM82, such as RM82:A6OCB = 1:9 denoted by blue circles and RM82:A6OCB:EHA = 1.7:3.4:4.9 denoted by black squares in Fig. 3(a), the degree of polymerization grows faster. This is due to the longer chain of RM82 compared to other monomers, as shown in Fig. 1(a), making RM82 difficult to move in solutions and thus slowing down the reactions between acrylates. The degree of polymerization curves of the 1000-monomer models shows a bilinear feature. In contrast, the larger model with 10,000 monomers has polymerization and crosslinking reactions proceed relatively slowly. All models' degree of polymerization reaches ~ 90% within 30 ns. The different molar percentages of RM82 also influence the crosslink density, shown in Fig. 3(b). Here, we treat the LCE models as side-chain systems with acrylate backbones and RM82 crosslinkers, so the number

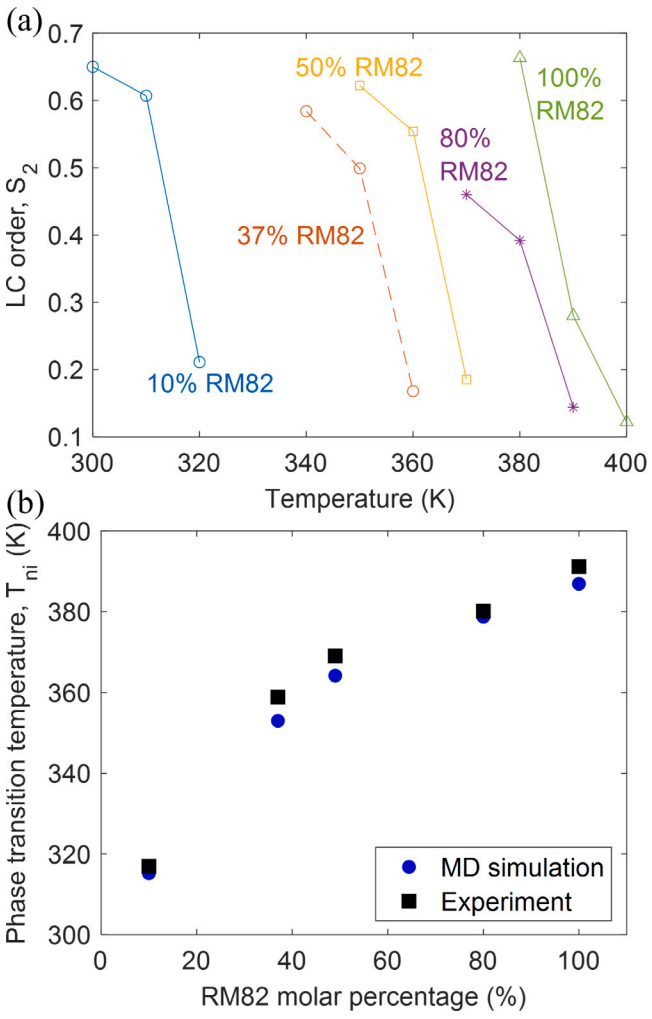

Fig. 2. (a) The evolution of LC orders, S_2, at different temperatures for A6OCB and RM82 monomer mixtures with different molar percentages of RM82; (b) the nematic–isotropic transition temperatures of monomer mixtures estimated at $S_2 = 0.4$ based on data in (a) compared against experimental data (Jull et al., 2022).

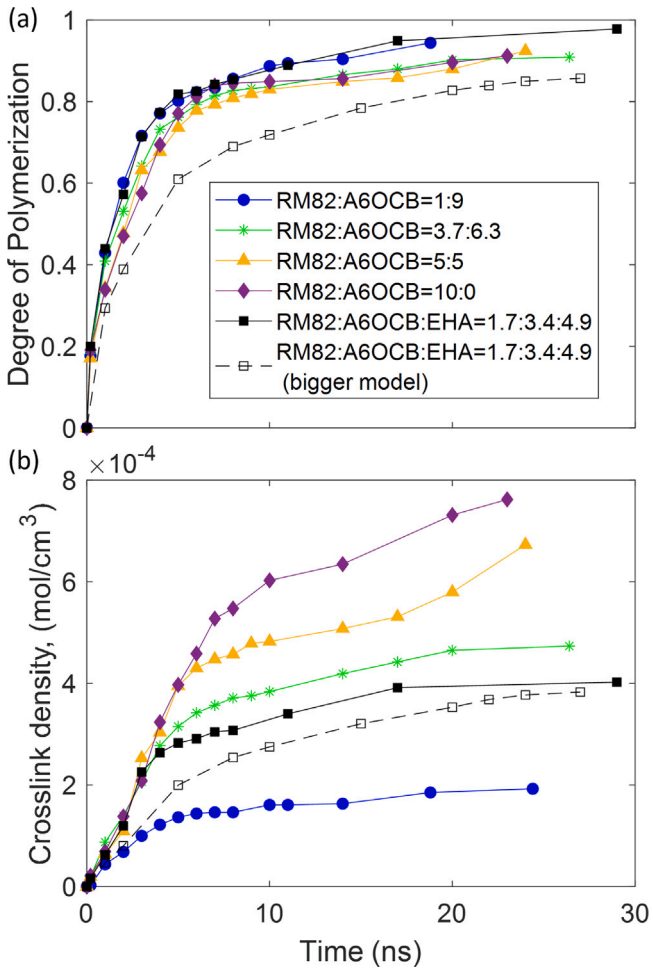

Fig. 3. The evolution of (a) the degree of polymerization and (b) crosslinking density during MD simulations of polymerization and crosslinking for nematic LCEs with different compositions.

of reacted RM82 crosslinkers per unit volume is calculated as the crosslink density. While the larger model has a relatively lower degree of polymerization than the 1000-monomer model with the same composition, they reach nearly the same crosslinking density ~ 4 mol/cm^3 in their final nematic LCE models. As demonstrated in many studies, the crosslinking densities play a decisive role in many properties of LCE systems (Ren et al., 2009; Brighenti and Cosma, 2021). Hence, while having different reaction progresses, the LCE models of 1000 and 10,000 monomers should have consistent final molecular structures and properties.

Fig. 4(a) displays the atomistic configurations of the nematic LCE systems with different compositions at 300 K. The rod-shaped rigid part of RM82 and A6OCB are represented by blue and red ellipsoids, respectively, and the remaining atoms forming flexible chains are represented by gray spheres. Due to the applied electrical fields during polymerization and crosslinking, all the nematic LCEs have their directors in the x-direction. Fig. 4(b) shows the acrylate atoms only, where red atoms represent the polymerized acrylate atoms on backbones and green atoms represent the unreacted sites. Note that the 1000-monomer models in Fig. 4 have different sizes due to their different compositions. For the convenience of visualization, they are scaled to the same size in Fig. 4. The nematic LCE models have the LC order, S_2, ranging from 0.7 and 0.8. To account for the polydispersity of the chain lengths between crosslinks, we calculate the polydispersity index, $PDI = M_w/M_n$ where M_w is the weight average molecular weight and M_n the number average molecular weight. The LCE model with 10% RM82 has the highest PDI of 1.62. With increased RM82, the PDI monotonically drops. The low values of PDI indicate relatively uniform chain lengths between crosslinks.

Fig. 5 presents the calculated glass transition temperatures, T_g, of the nematic LCE models and their comparison with experiments. In MD simulations, T_g is determined by (i) plotting the density vs. temperature data points and (ii) finding the temperature at the intersection of the bilinear curve from the density vs. temperature data (Jull et al., 2022; Prathumrat et al., 2021). When the molar percentage of RM82 increases, T_g generally increases except for the LCE model containing EHA. EHA monomers have been added in experimental studies to increase the flexibility of the polymer chains and thus lower the T_g (Mistry et al., 2018a). Such an effect is well captured by our atomistic model. Furthermore, increasing the degree of polymerization also increases T_g. In summary, our MD simulations of acrylate LCEs predict T_g values with good accuracy.

3. Results and discussion

3.1. Spontaneous deformations and shape memory

The ability of thermotropic nematic LCEs to deform spontaneously and exhibit a shape memory effect relies on their transition between

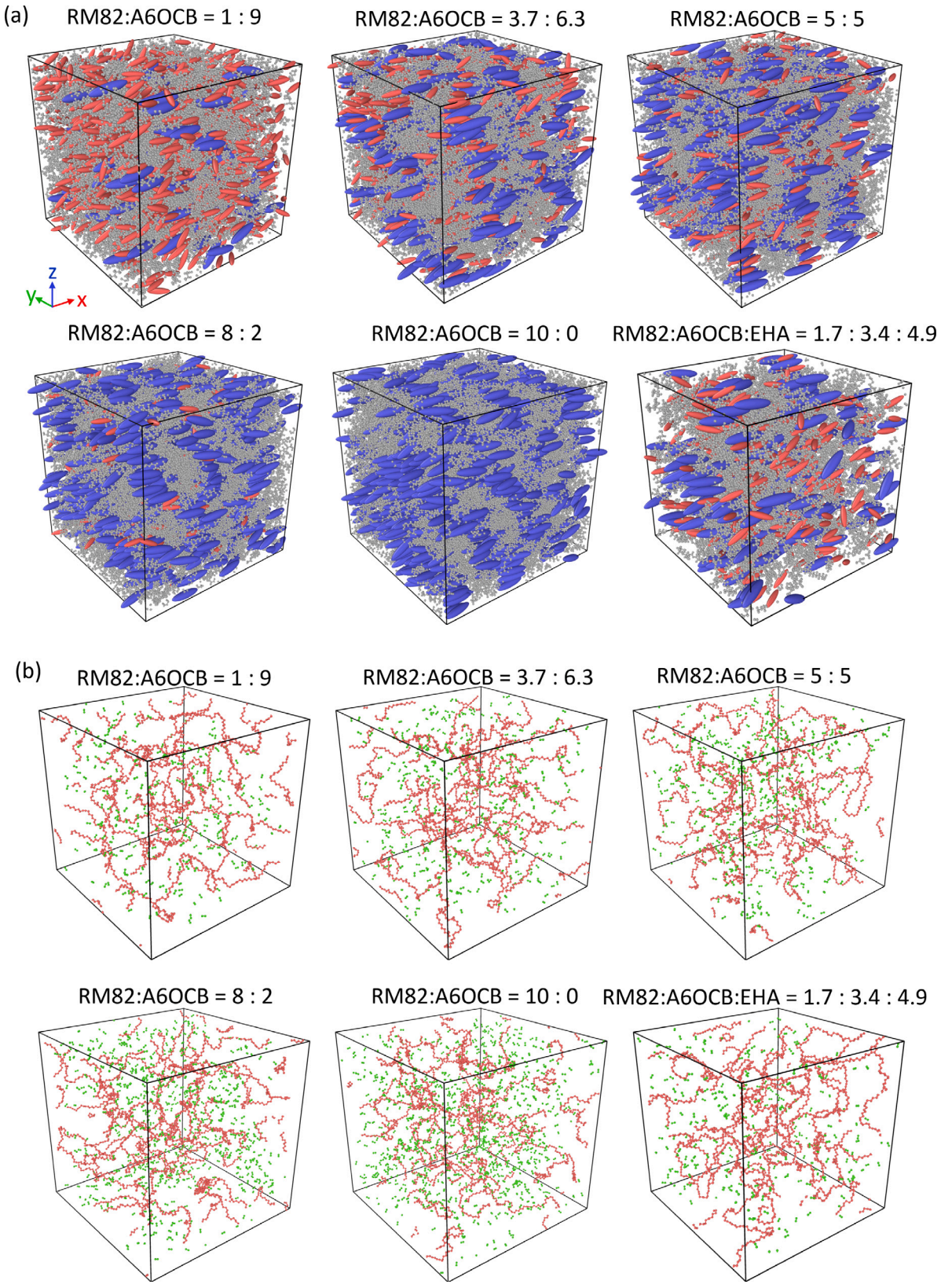

Fig. 4. (a) Atomistic configurations of nematic LCEs with different molar ratios of RM82, A6OCB, and EHA monomers where the rod-shaped rigid groups in RM82 and A6OCB mesogens are represented by blue and red ellipsoids, respectively, as shown in Fig. 1(a), and the remaining atoms forming flexible chains are represented by gray spheres; (b) polymerized backbone atoms (red) and unreacted acrylate C=C atoms (green) for the 6 LCE models.

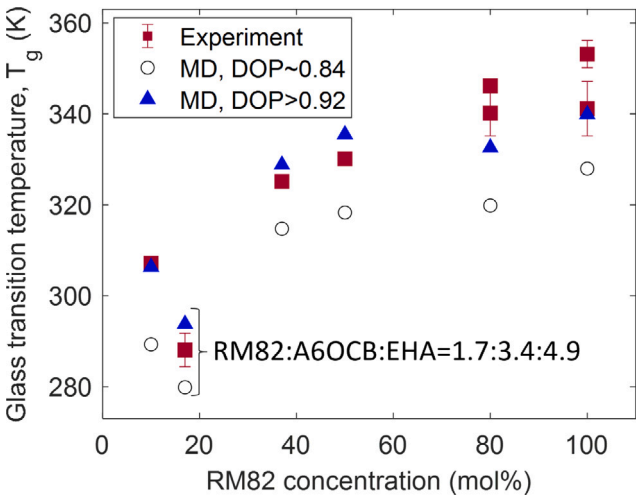

Fig. 5. The glass transition temperatures of the 6 nematic LCE models in Fig. 4 with different degrees of polymerization predicted by MD simulations compared against experiments (Jull et al., 2022).

the nematic and isotropic phases during heating and cooling. At lower temperatures, these LCEs exist in a nematic state, where mesogens align along a defined director, maintaining order. Heating disrupts this order, shifting the LCEs into an isotropic phase where mesogens lose alignment. In our LCE system, heating causes a shrinkage along the director's dimension and expansion in the other dimensions. Upon cooling, this process reverses, allowing the LCEs to revert to the original shape by 'remembering' the configuration imprinted by the mesogens within the polymeric network. Although these behaviors are commonly observed in experiments, replicating them accurately using MD simulations presents a challenge. Here, we introduce MD simulations aimed at replicating and studying the spontaneous deformations and shape memory effects observed in acrylate LCEs.

Fig. 6(a) presents the strain evolution of the nematic LCE model (blue round markers) with the molar ratio of RM82:A6OCB = 5:5 during heating from 300 K to 600 K. The nematic LCE model at 300 K is in a nearly cubic configuration with three edge lengths, l_x = 92.12 Å, l_y = 89.72 Å, l_z = 90.37 Å. Then, for each 50 K increment, the LCE model is equilibrated at a constant temperature and zero pressure for at least 20 ns until no visible change in model sizes and S_2 can be detected. At 450 K, l_x = 87.45 Å, l_y = 91.66 Å, l_z = 100.61 Å, corresponding to $\epsilon_{xx} = -5.08\%$ and $1/2(\epsilon_{yy} + \epsilon_{zz}) = 4.36\%$. The strain evolution during the heating process predicted by MD simulations is in excellent agreement with experiment data (red square markers) in Fig. 6(a) (Jull et al., 2022). In particular, 350 K is a threshold temperature at which significant deformations start, demonstrating the remarkable accuracy of MD simulations compared to experiments. The uniaxial order, S_2, predicted by MD simulations, drops from 0.78 to 0.45 (blue round markers) vs. the drop from 0.62 to 0.50 in experiments (red square markers) in Fig. 6(b) during the heating from 300 K to 450 K. Thus, S_2 shows a qualitative agreement between MD simulations and experiments. The quantitative discrepancy can be caused by a few factors. Firstly, despite our efforts to replicate the polymerization and crosslinking procedures in experiments, our simulations cannot capture all the details. For instance, different methods for aligning mesogens are employed in experiments (surface rubbing) and simulations (electric field), leading to potential discrepancies in the crosslinking topology between our atomistic models and actual experimental conditions. Secondly, variations in time and size scales between simulations and experiments can also contribute to disparities in S_2. The process-structure–property correlation for LCEs can be an interesting topic for future investigation with MD simulations. We further heat the LCE model in MD simulations to 600 K. The results of strains vs. temperatures in Fig. 6(a) show an increasing slope when the temperature gets higher, while the results of S_2 vs. temperatures in Fig. 6(b) show a larger slope in the intermediate-temperature region. Thus, the shape changes and the nematic order are not highly consistent in our MD simulations. The correlation between spontaneous deformations and nematic order needs further investigation. The first two columns in Fig. 7 show the mesogen configurations of the LCE model at 300 K and 600 K, respectively. The alignment of mesogens along the x-direction at 300 K exhibits the nematic phase, while the mesogens at 600 K become more randomly orientated. By contrast, the RM82 mesogens of the blue ellipsoids at 600 K in Fig. 7 still display some alignment along the x-direction compared to the A6OCB mesogens of the red ellipsoids, contributing to the value of $S_2 = 0.25$. This is not surprising since, when we calculate T_{ni} for A6OCB and RM82 monomers for PCFF validation in the previous section, we notice that RM82 monomers take 20–30 ns to reach equilibrium during phase transition, compared to 3–5 ns for A6OCB monomers. In the crosslinked LCE, the motion of RM82 mesogens is further restricted, and thus they take longer time to become stable during the phase transition at 600 K. The LCE model at 600 K in Fig. 7 is obtained after MD simulation of equilibration at 600 K for 60 ns, which is negligibly short compared to the time duration up to a few minutes or even hours in experiments to observe natural deformations. Therefore, long-time MD simulations are important to fully capture the heat-induced spontaneous deformations of nematic LCEs.

In contrast to the spontaneous deformation during heating, the isotropic-to-nematic transition at cooling and the resulting shape changes back to its original state are more challenging to model by MD simulations. Appropriate selection of force fields and modeling of molecular structures is critical for realizing the disorder-to-order transition and the shape memory effect. Fig. 6(c) shows the strain evolution during the cooling of the isotropic LCE model obtained from the previous heating process. Starting from 600 K, the isotropic LCE model is equilibrated at a constant temperature and zero pressure with a 50 K decrement. The equilibration at each temperature is maintained for 50 ns to achieve a stable size. During the cooling from 600 K to 300 K, the average strain along the y and z-directions shows a 16.38% recovery perpendicular to the director, and ϵ_{xx} shows a 11.89% strain recovery along the director, as displayed in Fig. 6(c). Simultaneously, the uniaxial order S_2 increases from ~0.25 to ~0.45. Note that the smallest S_2 we can obtain at 600 K is 0.22, which is not fully isotropic. Our primary interest here is to observe the shape changes back to the nematic phase from an isotropic state to validate the shape memory effect of our MD models. Thus, we further heat the LCE model from 600 K to 800 K, at which temperature, an even lower $S_2 \sim 0.14$ is obtained with a larger spontaneous deformation compared to the original nematic LCE at 300 K. In reality, the acrylate LCEs in our studies should decompose when subjected to high temperatures up to 800 K. So, the 800 K heating process here merely aims to achieve a more isotropic LCE model, which will take time beyond the limit of MD simulations at 600 K. Using a similar cooling procedure, the strain and S_2 changes are more significant than the cooling from 600 K to 300 K. The average of ϵ_{yy} and ϵ_{zz} shows a 26.93% strain recovery perpendicular to the director, and ϵ_{xx} shows 13.82% strain recovery along the director. The directions perpendicular to the initial director show a better shape memory effect.

Fig. 7 depicts the mesogen configurations and the overall model sizes at different temperatures during heating and cooling, where we can track the shape memory behavior and the changes in mesogen orientations. Many nematic LCEs show a sharp transition in deformations and the LC order at T_{ni} (Clarke et al., 2001; Warner, 2007), which has also been captured by coarse-graining MD simulations (Ilnytskyi et al., 2012). In contrast, our study reveals a distinctive behavior: both deformations and the S_2 exhibit gradual evolution during the heating and cooling process, in agreement with experimental findings

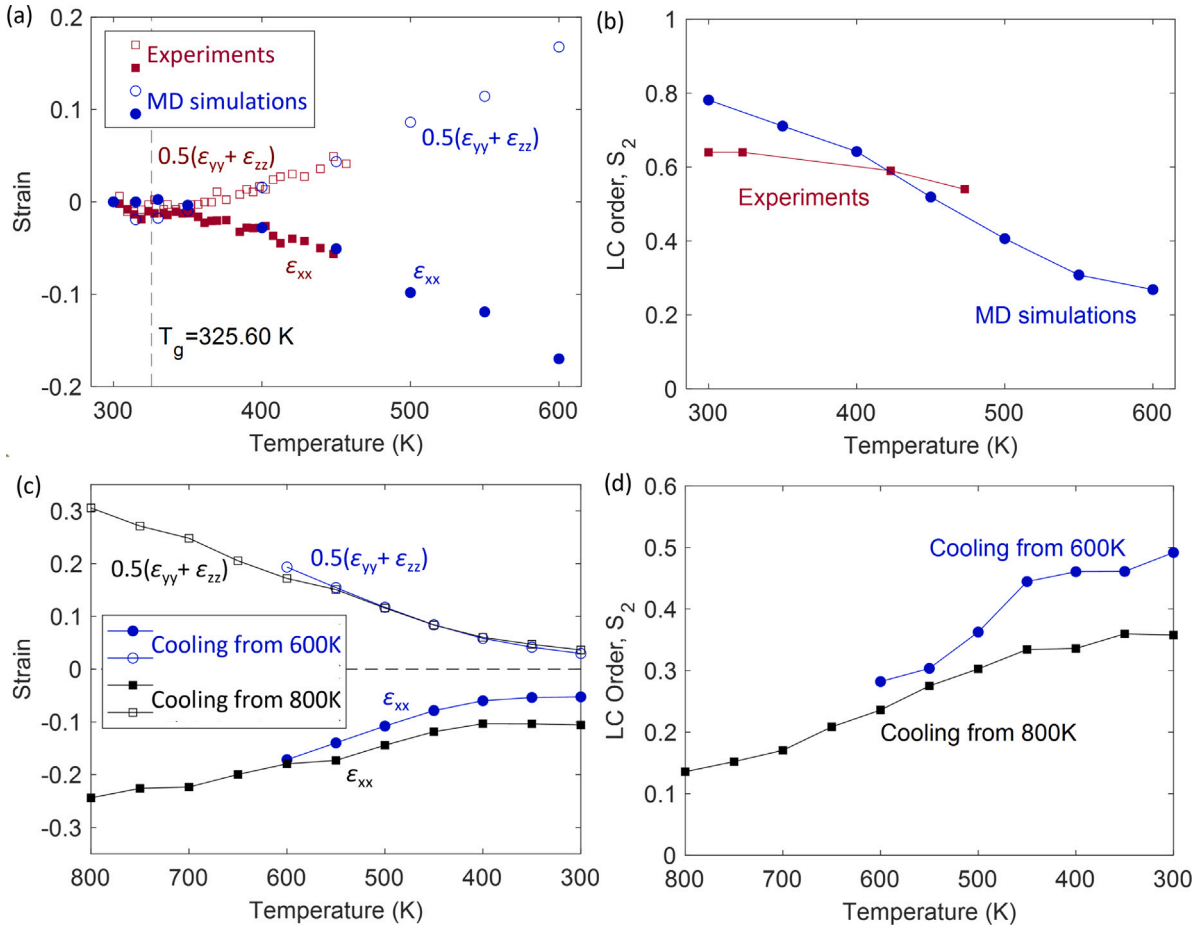

Fig. 6. When heating from 300 K to 600 K the nematic LCE model with molar ratio, RM82:A6OCB = 5:5, (a) the strain changes along the director (x direction) and perpendicular to the director, and (b) the evolution of uniaxial order, S_2, predicted by MD simulations in comparison with experiments. When cooling the same LCE model from 600 K and from 800 K, respectively, (c) the strain changes along the director (x direction) and perpendicular to the director, and (d) the evolution of uniaxial order, S_2, predicted by MD simulations.

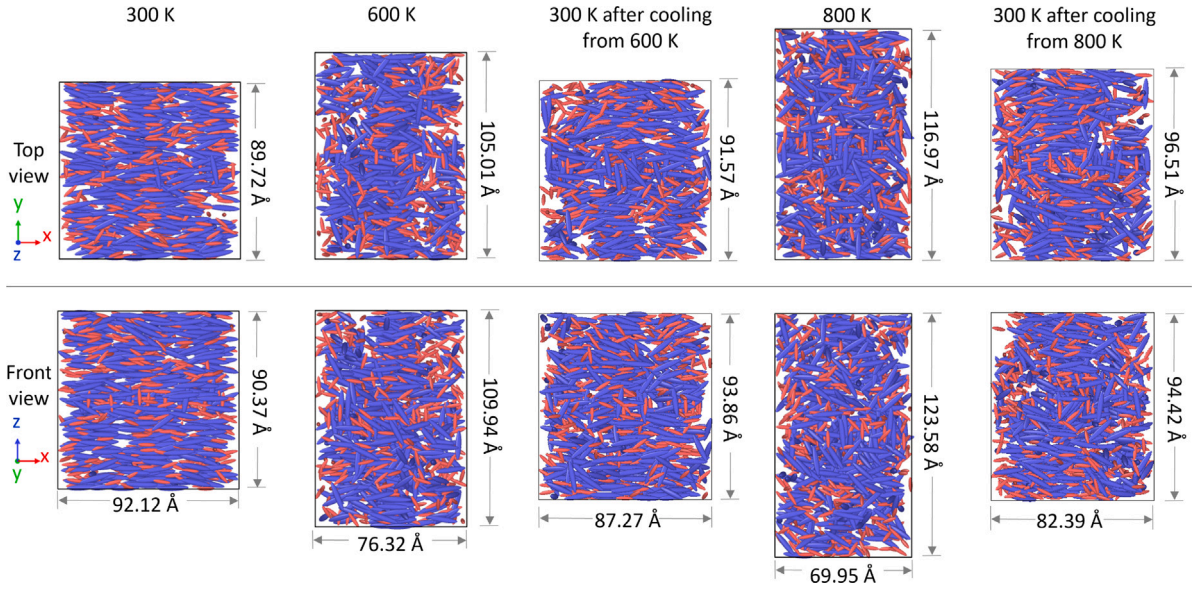

Fig. 7. The top view (xy plane) and the front view (xz plane) of mesogen configurations for the LCE model at 300 K, at 600 K, at 300 K after cooling from 600 K, at 800 K, and at 300 K after cooling from 800 K, which demonstrate the shape-memory behavior of nematic LCEs upon heating and cooling.

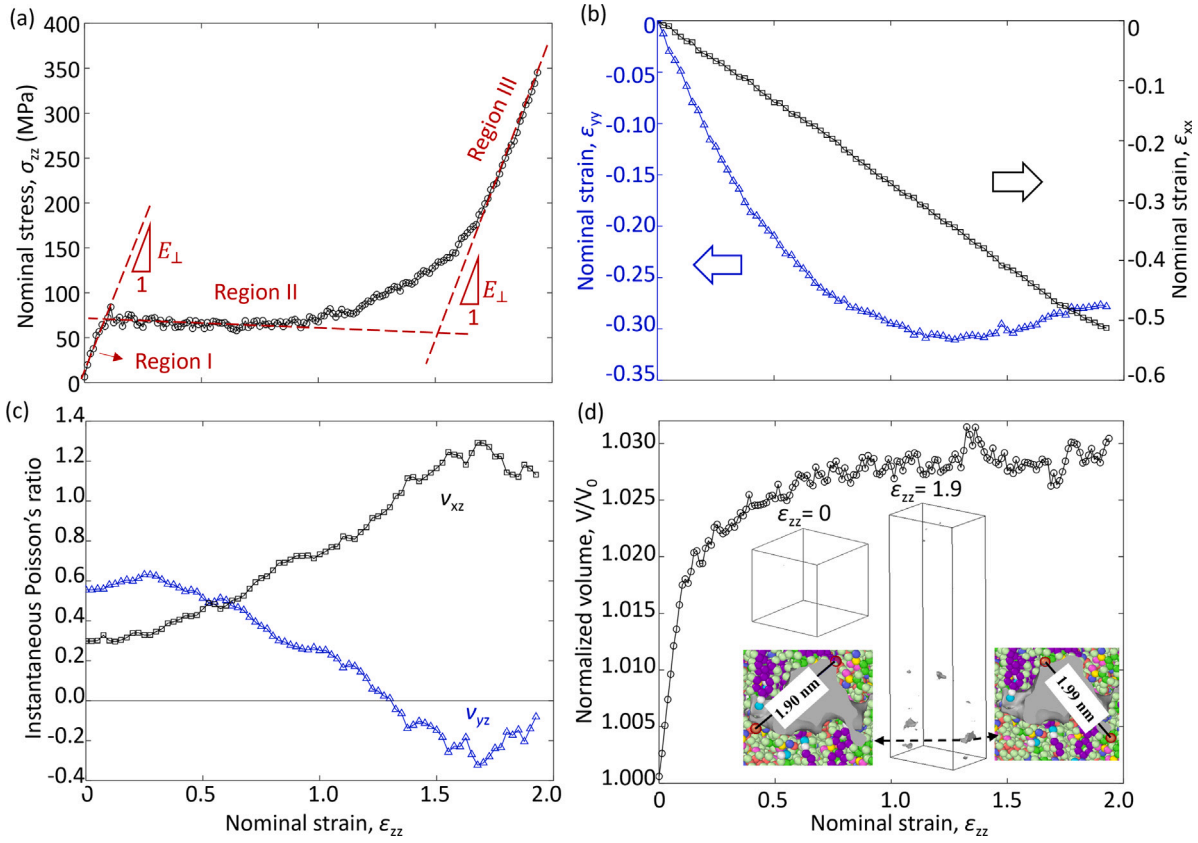

Fig. 8. When stretching the nematic LCE model in the direction (z) perpendicular to the director (x), (a) the nominal stress σ_{zz} vs. nominal strain ϵ_{zz} curves show three regions; (b) the nominal strain ϵ_{xx} denoted by black squares monotonically decreases with the stretch along z and the nominal strain ϵ_{yy} denoted by blue triangles first decreases then increases with the stretch; (c) the instantaneous Poisson ratios vs. nominal strain ϵ_{zz} curves show negative ν_{xz} when $\epsilon_{zz} > 1.35$; (d) the volumetric evolution of the LCE model and the voids within the LCE model before and after uniaxial tension show negligible porosity effect.

on acrylate LCEs of a similar nature (Mistry et al., 2018b; Jull et al., 2022). Consequently, estimating T_{ni} based on our MD simulations is challenging. The widely accepted Maier–Saupe theory (Luckhurst and Zannoni, 1977), which establishes a critical S_2 value of 0.4 for the nematic–isotropic transition in low molar mass liquid crystals, is not directly applicable to LCEs. Besides, the cause of the residual S_2 at 800K and its influence on phase transition remains to be further investigated.

There have been discussions on whether one should treat the acrylate LCEs and other similar LCEs as: (i) side-chain LCEs with polyacrylate backbone and RM82 crosslinkers or (ii) main-chain LCEs backboned by RM82 chains. MD models allow us to calculate the radius of gyration, which can help to elucidate the molecular topology. The shape changes observed in our MD simulations indicate that the radius of gyration parallel to the director, $R_\parallel$, should be larger than the radius of gyration perpendicular to the director, $R_\perp$. However, when calculating the radius of gyration using the acrylate backbones, $R_\parallel$ = 153 Å, smaller than $R_\perp$ = 214 Å, which conflicts with the shape changes in our MD simulations. By following Kramers' Theorem (Rubinstein and Ralph, 2003) and treating the LCE as a branched system, we obtain $R_\parallel/R_\perp$ = 1.62 with $R_\parallel$ = 1174.15 Å and $R_\perp$ = 724.03 Å, which is qualitatively consistent with the shape changes in our MD simulations. The relatively low anisotropy of R_g and the complicated crosslinking topology created by RM82 indicate that our LCE model has a mixture of main-chain and side-chain crosslinking structure.

3.2. Mechanical behavior and auxetic effect

The mechanical behavior of a nematic LCE under the uniaxial tension perpendicular to the director has been extensively studied experimentally and theoretically. Generally, during uniaxial extension, LCEs demonstrate soft elasticity representing low-resistance liquid-like deformations. Recent experiments have observed the instantaneous negative Poisson's ratio in acrylate LCEs, i.e., an auxetic behavior. This section introduces our MD simulations of the soft elasticity and auxetic behavior of LCEs under uniaxial tension perpendicular to the initial director.

Fig. 8(a) presents the nominal stress σ_{zz} vs. nominal strain ϵ_{zz} when the nematic LCE with the composition RM82:A6OCB = 5:5 is stretched at 300 K in the z-direction, perpendicular to the initial director along the x-direction. During the tension test, a constant strain rate of $\dot{\epsilon}_{zz}$ is used while x and y dimensions are adjusted to maintain $\sigma_{xx} = 0$ and $\sigma_{yy} = 0$ by adopting the NPT ensemble in MD simulations. The highly nonlinear stress–strain curve can be divided into three regions. To identify the critical stretch ratios between different regions where the stretch ratio $\lambda = 1 + \epsilon_{zz}$, we use the intersection of the linear curves between two neighboring regions. Region I resembles the mechanical behavior of isotropic rubber under uniaxial tension, ending at the stretch ratio λ_1 = 1.09; Region II shows a significantly decreased stiffness due to the rotation of mesogens, ending at λ_2 = 2.53; with the director now aligning in the stretch direction of z, Region III sees a return to the stiffer mode. The threshold between Regions I and II and the subsequent large plateau in Region II is very similar to the experimentally observed stress–strain curves of highly anisotropic main-chain LCEs (Clarke et al., 2001; Biggins et al., 2008). Using the critical stretch ratios, we can estimate the anisotropy of the step-length tensor, $r = (\frac{\lambda_2}{\lambda_1})^2$ = 5.39. Then, we can obtain the thermally induced length changes, $\lambda_m = r^{1/3}$ = 1.75, larger than what we observe in Fig. 6(c). Regions I and III have an identical slope in our MD simulations, representing Young's modulus, $E_\perp$ = 700 MPa. Compared to Young's modulus and stress levels up to a few MPa in experiments, the higher

magnitudes predicted in our MD simulations are attributed to the high strain rate of 2.5×10^8 s^{-1} and the temperature of 300 K below its T_g. Therefore, long-time MD simulations capable of modeling tension tests and heating-cooling processes over several hours would be valuable to validate these LCE models.

Fig. 8(b) displays the evolution of nominal strains ϵ_{yy} and ϵ_{xx} during the uniaxial tension along z. While ϵ_{xx} decreases in a linear mode with respect to ϵ_{zz}, ϵ_{yy} reaches a minimum of −0.3 at $\epsilon_{zz} = 1.25$ and then starts to increase. Physically, it means that the thickness in the y-direction decreases and then increases, resembling what has been observed in experiments for the so-called auxetic effect. Based on the strain evolution, the instantaneous Poisson ratios, $\nu_{xz} = -d\epsilon^t_{zz}/d\epsilon^t_{xx}$ and $\nu_{yz} = -d\epsilon^t_{zz}/d\epsilon^t_{yy}$ can be calculated where the incremental true strain $d\epsilon^t_{ii} = d\ \ln(1+\epsilon_{ii})$. The results in Fig. 8(c) confirm that negative directional Poissons's ratio occurs during the uniaxial tension process.

Earlier experimental studies have proposed that the auxetic response of LCEs is not driven by void generation but is an intrinsic material behavior (Mistry et al., 2018a). Here, we track atomistic configurations in MD simulations to validate the underlying mechanism of auxetic behavior. To perform porosity analysis, the Gaussian density method is used with a radius scaling factor of 150% and an iso-value of 0.1 (Krone et al., 2012), such that the model at $\epsilon_{zz} = 0$ is void-free, as shown in Fig. 8(d). When stretched up to $\epsilon_{zz} = 1.9$, the LCE model shows voids denoted by the gray regions in Fig. 8(d). A closer look at the largest void in Fig. 8(d) reveals that the longest diameter is less than 2 nm; thus, the voids generated within LCEs are negligibly small. This is consistent with the AFM measurements showing that no voids larger than 5 nm (the limit of AFM measurements) are generated in the acrylate LCEs during their auxetic behavior. Fig. 8(d) suggests that the volume of the LCE model stays nearly constant from $\epsilon_{zz} = 1.0$ during which the auxetic behavior occurs. Therefore, we conclude that the auxetic effect observed in our MD simulations of acrylate LCEs is indeed an intrinsic material behavior at the molecular level.

Using MD models, we track the mesogen rotation under the uniaxial tension. Fig. 9(a) presents the angle of the director with respect to the z axis at different ϵ_{zz} during the uniaxial tension. The director orientation is determined by solving for the eigenvector of the molecular order tensor in Eq. (1) corresponding to the largest eigenvalue. For the LCE model with RM82:A6OCB = 5:5, the director shows a sudden rotation at $\epsilon_{zz} = 1.25$ from the x- to the z-direction, similar to the mechanical-Fréedericksz transition, as reported by the 2D optical tracking of the director in experiments (Mistry et al., 2021). The sudden rotation of the director is consistent with the theoretical prediction for the uniaxial tension perpendicular to the initial director (Bladon et al., 1993). The uniaxial order for the LCE model with RM82:A6OCB = 5:5 in Fig. 9(b) presents a gradual decrease to $S_2 = 0.16$ at $\epsilon_{zz} = 1.25$ and then a gradual increase to $S_2 = 0.4$ at the end of the tension. Such a process can be visualized in the mesogen configurations in Fig. 9(c). The gradual transition of S_2 during uniaxial tension has been observed experimentally for a similar acrylate LCE (Haruko and Kenji, 2013). Also indicated in Fig. 9(a–b) is that, when tuning the molar ratios of A6OCB and RM82 in LCEs, we can adjust the critical stretch ratio where the director rotation and auxetic effect occur. When A6OCB dominates the composition, the critical stretch ratio happens earlier where the sudden rotation of the director and the minimum S_2 can be identified, compared to the model with 100% RM82. Such a composition-dependent behavior can be explained in two aspects: (i) the smaller A6OCB mesogens make them easier to rotate under uniaxial tension, and thus, when A6OCB dominates in LCEs, the sudden rotation of mesogens happens earlier; (ii) RM82 have reactive sites on both ends and thus a high molar percentage of RM82 generates a higher crosslink density, making LCEs more resistance to mesogen rotations. Thus, the size of the mesogens and the crosslinking topology are critical for the LCE mechanical properties and the modeling of the mechanics of LCEs.

Biaxial order parameters have been proposed to be relevant for the emergence of auxetic behavior, according to the experimental

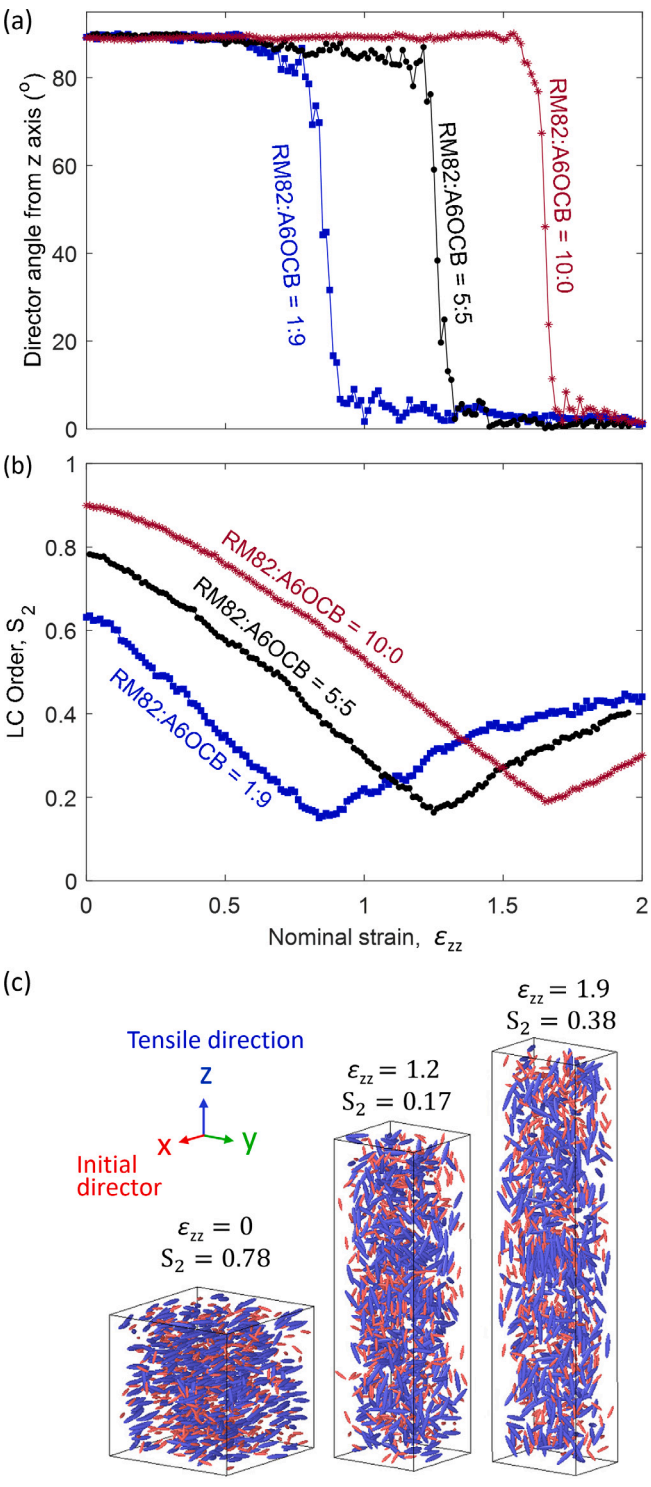

Fig. 9. During the uniaxial tension of LCE models with different compositions (molar ratio RM82:A6OCB = 1:9, RM82:A6OCB = 5:5, RM82:A6OCB = 10:0) along the z-direction, (a) the director angle from the z-axis shows a sudden change, (b) the uniaxial order S_2 first decrease up to the nearly isotropic state and then increase, and (c) the atomistic configurations for the LCE model with RM82:A6OCB = 5:5 at different strains show that mesogens start from the alignment in the x-direction, become nearly isotropic and eventually align in the tensile direction along z.

studies (Raistrick et al., 2021; Wang et al., 2022). When all mesogens are symmetric about the director, we only have the uniaxial order, and the molecular order tensor in Eq. (1) becomes Diag$(-Q/2, -Q/2, Q)$ with the director aligning parallel to the z-axis and Q representing

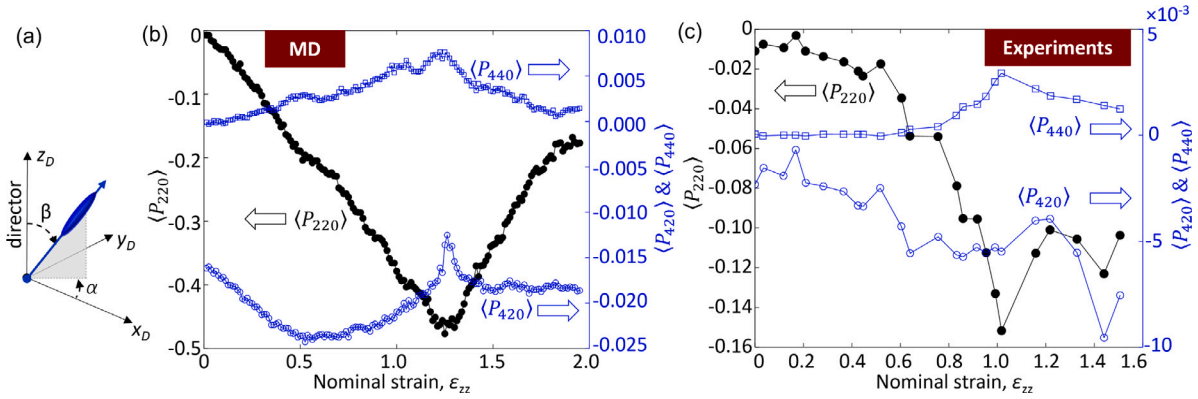

Fig. 10. (a) The schematics of the orientation of a mesogen in terms of the three principal directions with Z_D being the director and the evolution of biaxial order parameters during the uniaxial tensile test from (b) MD simulations and (c) experiments (Raistrick et al., 2021).

the uniaxial order parameter S_2 mentioned above. When there is no symmetry about the director, a biaxial order emerges and solving for the eigenvalues of the molecular order tensor in Eq. (1) leads to

$$\mathbf{Q} = \begin{bmatrix} -(Q-b)/2 & 0 & 0 \\ 0 & -(Q+b)/2 & 0 \\ 0 & 0 & Q \end{bmatrix}, \tag{2}$$

where b is the biaxial order parameter. Using the Raman spectroscopy, b can be measured as $\langle P_{220}\rangle = \frac{3}{2}\langle(1-\cos^2\beta)\cos(2\alpha)\rangle$, in addition to the other biaxial order parameters $\langle P_{420}\rangle = \frac{1}{24}\langle(7\cos^2\beta-1)(1-\cos^2\beta)\cos(2\alpha)\rangle$ and $\langle P_{440}\rangle = \frac{1}{16}\langle(1-\cos^2\beta)^2\cos(4\alpha)\rangle$, where α and β determine the orientation of one mesogen, as shown in Fig. 10 with x_D, y_D and z_D being the three principal directions corresponding to the three eigenvalues in Eq. (2). The three biaxial order parameters are determined for the nematic LCE model in our MD simulations, as presented in Fig. 10(b). The evolution of $\langle P_{220}\rangle$ and $\langle P_{440}\rangle$ in Fig. 10(b) during the uniaxial tension perpendicular to the initial director exhibit qualitative agreement with the Raman spectroscopy measurements in Fig. 10(c) (Raistrick et al., 2021): $\langle P_{220}\rangle$ drops to a negative value during the tension up to $\epsilon_{zz} = 1.25$ where the instantaneous auxetic behavior initiates, and then starts to increase; $\langle P_{440}\rangle$ shows relatively smaller changes along the positive direction during uniaxial tension and a peak value is recorded at $\epsilon_{zz} = 1.25$. In our MD simulations, $\langle P_{420}\rangle$ fluctuates between −0.01 and −0.025 while $\langle P_{420}\rangle$ in experiments drops in a consistent mode. Besides, the biaxial order in our MD simulations does not disappear immediately after the director rotation at $\epsilon_{zz} = 1.25$, which is also consistent with experimental observations. Thus, our MD simulations well capture the emergence of biaxial order during uniaxial tension perpendicular to the initial director and confirm the relation between biaxial order and the auxetic response. Further insight is required to understand the microscopic mechanism which leads to the biaxial ordering and the auxetic response, however, the first step towards simulating these systems using an all-atomistic approach has now been undertaken.

4. Conclusions

Our study leverages PCFF-based all-atom MD simulations to replicate the physical behavior of a particular class of nematic LCEs. The modeling of the polymerization and crosslinking processes has proven robust, accurately capturing the synthesis history- and composition-dependent glass transition temperatures of the LCEs. The MD models match experimental observations well, demonstrating consistency both in shape changes due to temperature variations and the manifestation of auxetic behavior under uniaxial tensile load. Notably, our simulations replicate the isotropic-to-nematic phase transition during cooling and the simultaneous restoration of the original shape, a conventional challenge to all-atom MD simulations. Auxetic responses have only been found in one category of acrylate LCEs and, thus, are not a universal LCE property. Reproducing auxeticity in our LCE models demonstrates the robustness of our all-atom MD modeling framework for capturing composition-dependent behaviors. Using atomistic LCE models, we can identify critical factors such as the radius of gyration and the biaxial order parameters in relation to the macroscopic behavior of LCEs.

The framework we establish for all-atom MD simulations of LCEs not only fosters a mechanistic understanding of their behavior but also facilitates the development of composition-specific models regarding the mechanics and the computational design of LCEs. However, to fully realize the potential of all-atom MD modeling, it becomes imperative to develop long-time simulations that align with the temporal scales of physical experiments. Bridging this gap would significantly enhance the utility and accuracy of the MD framework, advancing our comprehension and predictive capacity concerning the physical understanding of nematic materials.

Funding

This work was supported by the National Science Foundation, United States [grant number NSF-CMMI-2138431] and the Presidential Doctoral Research Fellowship of Utah State University, United States.

Declaration of competing interest

The authors declare that they have no known competing financial interests or personal relationships that could have appeared to influence the work reported in this paper.

Data availability

The data for this research are openly available at https://doi.org/10.26078/6170-d520.

Acknowledgments

The authors thank Dr. Devesh Mistry from the University of Leeds for discussions on LCE synthesis. The support and resources from the Center for High Performance Computing at the University of Utah are gratefully acknowledged.

References

Allen, M.P., Warren, M.A., Wilson, M.R., Sauron, A., Smith, W., 1996. Molecular dynamics calculation of elastic constants in Gay–Berne nematic liquid crystals. J. Chem. Phys. 105 (7), 2850–2858.

Biggins, J., Terentjev, E., Warner, M., 2008. Semisoft elastic response of nematic elastomers to complex deformations. Phys. Rev. E 78 (4), 041704.

Bladon, P., Terentjev, E., Warner, M., 1993. Transitions and instabilities in liquid crystal elastomers. Phys. Rev. E 47 (6), R3838.

Boyd, N.J., Wilson, M.R., 2015. Optimization of the GAFF force field to describe liquid crystal molecules: the path to a dramatic improvement in transition temperature predictions. Phys. Chem. Chem. Phys. 17 (38), 24851–24865.

Brighenti, R., Cosma, M.P., 2021. Smart actuation of liquid crystal elastomer elements: cross-link density-controlled response. Smart Mater. Struct. 31 (1), 015012.

Brown, W.M., Petersen, M.K., Plimpton, S.J., Grest, G.S., 2009. Liquid crystal nanodroplets in solution. J. Chem. Phys. 130 (4).

Cheung, D., Clark, S., Wilson, M.R., 2002. Parametrization and validation of a force field for liquid-crystal forming molecules. Phys. Rev. E 65 (5), 051709.

Clarke, S., Hotta, A., Tajbakhsh, A., Terentjev, E., 2001. Effect of crosslinker geometry on equilibrium thermal and mechanical properties of nematic elastomers. Phys. Rev. E 64 (6), 061702.

de Haan, L.T., Schenning, A.P., Broer, D.J., 2014. Programmed morphing of liquid crystal networks. Polymer 55 (23), 5885–5896.

Gissinger, J.R., Jensen, B.D., Wise, K.E., 2017. Modeling chemical reactions in classical molecular dynamics simulations. Polymer 128, 211–217.

Gissinger, J.R., Jensen, B.D., Wise, K.E., 2020. Reacter: A heuristic method for reactive molecular dynamics. Macromolecules 53 (22), 9953–9961.

Guo, Y., Zhang, J., Hu, W., Khan, M.T.A., Sitti, M., 2021. Shape-programmable liquid crystal elastomer structures with arbitrary three-dimensional director fields and geometries. Nature Commun. 12 (1), 5936.

Haruko, H., Kenji, U., 2013. Nonuniform and uniform deformations of stretched nematic elastomers.

Hussain, M., Jull, E.I.L., Mandle, R.J., Raistrick, T., Hine, P.J., Gleeson, H.F., 2021. Liquid crystal elastomers for biological applications. Nanomaterials 11, 813.

Ilnytskyi, J.M., Neher, D., 2007. Structure and internal dynamics of a side chain liquid crystalline polymer in various phases by molecular dynamics simulations: A step towards coarse graining. J. Chem. Phys. 126 (17).

Ilnytskyi, J.M., Saphiannikova, M., Neher, D., Allen, M.P., 2012. Modelling elasticity and memory effects in liquid crystalline elastomers by molecular dynamics simulations. Soft Matter 8 (43), 11123–11134.

Jull, E.I., Mandle, R.J., Raistrick, T., Zhang, Z., Hine, P.J., Gleeson, H.F., 2022. Toward in silico design of highly tunable liquid crystal elastomers. Macromolecules 55 (11), 4320–4330.

Kotikian, A., McMahan, C., Davidson, E.C., Muhammad, J.M., Weeks, R.D., Daraio, C., Lewis, J.A., 2019. Untethered soft robotic matter with passive control of shape morphing and propulsion. Science Robotics 4 (33), eaax7044.

Krone, M., Stone, J.E., Ertl, T., Schulten, K., 2012. Fast visualization of Gaussian density surfaces for molecular dynamics and particle system trajectories. EuroVis (Short Pap.) 10, 067–071.

Li, C., Liu, Y., Huang, X., Jiang, H., 2012. Direct sun-driven artificial heliotropism for solar energy harvesting based on a photo-thermomechanical liquid-crystal elastomer nanocomposite. Adv. Funct. Mater. 22 (24), 5166–5174.

Lide, D.R., 2004. CRC Handbook of Chemistry and Physics, vol. 85, CRC Press.

Luckhurst, G., Zannoni, C., 1977. Why is the Maier–Saupe theory of nematic liquid crystals so successful? Nature 267 (5610), 412–414.

Mihai, L.A., Mistry, D., Raistrick, T., Gleeson, H.F., Goriely, A., 2022. A mathematical model for the auxetic response of liquid crystal elastomers. Philos. Trans. R. Soc. A 380, 20210326.

Mihai, L.A., Raistrick, T., Gleeson, H.F., Mistry, D., Goriely, A., 2023. A predictive theoretical model for stretch-induced instabilities in liquid crystal elastomer. Liq. Cryst. 50, 1426–1438.

Mihai, L.A., Wang, H., Guilleminot, J., Goriely, A., 2021. Nematic liquid crystalline elastomers are aeolotropic materials. Proc. R. Soc. Lond. Ser. A Math. Phys. Eng. Sci. 477 (2253), 20210259.

Mistry, D., 2021. The richness of liquid crystal elastomer mechanics keeps growing. Liquid Cryst. Today 30, 59–66.

Mistry, D., Connell, S.D., Mickthwaite, S., Morgan, P.B., Clamp, J.H., Gleeson, H.F., 2018a. Coincident molecular auxeticity and negative order parameter in a liquid crystal elastomer. Nature Commun. 9 (1), 5095.

Mistry, D., Morgan, P.B., Clamp, J.H., Gleeson, H.F., 2018b. New insights into the nature of semi-soft elasticity and "mechanical-Fréedericksz transitions" in liquid crystal elastomers. Soft Matter 14 (8), 1301–1310.

Mistry, D., Traugutt, N.A., Sanborn, B., Volpe, R.H., Chatham, L., Zhou, R., Song, B., Yu, K., Long, K., Yakacki, C.M., 2021. Soft elasticity optimises dissipation in 3D-printed liquid crystal elastomers. Nature Commun. 12 (1), 6677.

Moon, J., Kim, B., Choi, J., Cho, M., 2019. Multiscale study of the relationship between photoisomerization and mechanical behavior of azo-polymer based on the coarse-grained molecular dynamics simulation. Macromolecules 52 (5), 2033–2049.

Park, S., Oh, Y., Moon, J., Chung, H., 2023. Recent trends in continuum modeling of liquid crystal networks: A mini-review. Polymers 15, 1904.

Prathumrat, P., Sbarski, I., Hajizadeh, E., Nikzad, M., 2021. A comparative study of force fields for predicting shape memory properties of liquid crystalline elastomers using molecular dynamic simulations. J. Appl. Phys. 129 (15).

Raistrick, T., Zhang, Z., Mistry, D., Mattsson, J., Gleeson, H.F., 2021. Understanding the physics of the auxetic response in a liquid crystal elastomer. Phys. Rev. Res. 3 (2), 023191.

Ren, W., McMullan, P.J., Griffin, A.C., 2009. Stress–strain behavior in main chain liquid crystalline elastomers: effect of crosslinking density and transverse rod incorporation on "Poisson's ratio". Phys. Status Solidi (b) 246 (9), 2124–2130.

Rogóż, M., Zeng, H., Xuan, C., Wiersma, D.S., Wasylczyk, P., 2016. Light-driven soft robot mimics caterpillar locomotion in natural scale. Adv. Opt. Mater. 4 (11), 1689–1694.

Rubinstein, M., Ralph, C., 2003. Polymer Physics. Oxford University Press.

Saed, M.O., Torbati, A.H., Nair, D.P., Yakacki, C.M., 2016. Synthesis of programmable main-chain liquid-crystalline elastomers using a two-stage thiol-acrylate reaction. JoVE (J. Vis. Exp.) (107), e53546.

Skačej, G., Zannoni, C., 2012. Molecular simulations elucidate electric field actuation in swollen liquid crystal elastomers. Proc. Natl. Acad. Sci. 109 (26), 10193–10198.

Skacej, G., Zannoni, C., 2014. Molecular simulations shed light on supersoft elasticity in polydomain liquid crystal elastomers. Macromolecules 47 (24), 8824–8832.

Soltani, M., Raahemifar, K., Nokhosteen, A., Kashkooli, F.M., Zoudani, E.L., 2021. Numerical methods in studies of liquid crystal elastomers. Polymers 13, 1650.

Stelzer, J., Longa, L., Trebin, H.-R., 1995. Molecular dynamics simulations of a Gay–Berne nematic liquid crystal: elastic properties from direct correlation functions. J. Chem. Phys. 103 (8), 3098–3107.

Stuart, M.A.C., Huck, W.T., Genzer, J., Müller, M., Ober, C., Stamm, M., Sukhorukov, G.B., Szleifer, I., Tsukruk, V.V., Urban, M., et al., 2010. Emerging applications of stimuli-responsive polymer materials. Nature Mater. 9 (2), 101–113.

Thompson, A.P., Aktulga, H.M., Berger, R., Bolintineanu, D.S., Brown, W.M., Crozier, P.S., in't Veld, P.J., Kohlmeyer, A., Moore, S.G., Nguyen, T.D., et al., 2022. LAMMPS-a flexible simulation tool for particle-based materials modeling at the atomic, meso, and continuum scales. Comput. Phys. Comm. 271, 108171.

Ula, S.W., Traugutt, N.A., Volpe, R.H., Patel, R.R., Yu, K., Yakacki, C.M., 2018. Liquid crystal elastomers: an introduction and review of emerging technologies. Liquid Cryst. Rev. 6 (1), 78–107.

Van Oosten, C., Harris, K., Bastiaansen, C., Broer, D., 2007. Glassy photomechanical liquid-crystal network actuators for microscale devices. Eur. Phys. J. E 23, 329–336.

Wang, Z., Raistrick, T., Street, A., Reynolds, M., Liu, Y., Gleeson, H.F., 2022. Direct observation of biaxial nematic order in auxetic liquid crystal elastomers. Materials 16 (1), 393.

Ware, T.H., McConney, M.E., Wie, J.J., Tondiglia, V.P., White, T.J., 2015. Voxelated liquid crystal elastomers. Science 347 (6225), 982–984.

Warner, 2007. Mark, and Eugene Michael Terentjev. Liquid Crystal Elastomers, vol. 120, Oxford University Press.

Warner, M., 2020. Topographic mechanics and applications of liquid crystalline solids. Annu. Rev. Condens. Matter Phys. 11, 125–145.

Warner, M., Terentjev, E.M., 2007. Liquid Crystal Elastomers, vol. 120, Oxford University Press.

White, T.J., Broer, D.J., 2015. Programmable and adaptive mechanics with liquid crystal polymer networks and elastomers. Nature Mater. 14 (11), 1087–1098.

Whitmer, J.K., Roberts, T.F., Shekhar, R., Abbott, N.L., De Pablo, J.J., 2013. Modeling the polydomain-monodomain transition of liquid crystal elastomers. Phys. Rev. E 87 (2), 020502.

Wilson, M.R., 1997. Molecular dynamics simulations of flexible liquid crystal molecules using a Gay-Berne/Lennard-Jones model. J. Chem. Phys. 107 (20), 8654–8663.

Wilson, M.R., 2005. Progress in computer simulations of liquid crystals. Int. Rev. Phys. Chem. 24 (3–4), 421–455.